SAXS Study of Oriented Crystallization of Polypropylene from a Quiescent Melt†

N. Stribeck,*,‡ U. Nöchel,‡ A. Almendárez Camarillo,‡ S. V. Roth,§ M. Dommach,§ and P. Bösecke⊥

Institute of Technical and Macromolecular Chemistry, University of Hamburg, Bundesstr. 45, 20146 Hamburg, Germany; HASYLAB at DESY, Notkestr. 85, 22603 Hamburg, Germany; and ESRF, 6 rue Jules Horowitz, B.P. 220, 38043 Grenoble Cedex 9, France

Received January 29, 2007; Revised Manuscript Received March 13, 2007

ABSTRACT: Uniaxially oriented polypropylene (PP) is molten in the synchrotron beam and crystallized from the quiescent melt, keeping its orientation in order to study the mechanisms of its crystallization. We document the different nanostructures observed as a function of melt-annealing temperature, undercooling, and time. In order to obtain a melt that crystallizes with high preferential orientation again, a melt-annealing temperature between 170 and 176 °C is chosen. Isothermal crystallization at 155 °C results in slow formation of (primary) lamellae placed at random. As the crystallization temperature is decreased (150, 145, and 140 °C), more and more secondary crystallites are observed which develop from a block mesostructure according to Strobl's mechanism. During the isothermal phase the blocks are fusing more or less to form imperfect lamellae. The structure evolution observed in the time-resolved small-angle X-ray scattering (SAXS) data during crystallization and remelting facilitates discrimination between the block structure and another frequently discussed morphology, Keller's cross-hatched structure. While after all our quiescent crystallization experiments most of the crystallites are blocks or incompletely fused lamellae, the hard-elastic precursor material which has been made under extreme gradients of temperature and pressure exhibits the melting of homogeneous and extended lamellae. As we apply a steep temperature gradient (−100 °C/min) to our melt in a nonisothermal crystallization experiment, we initially observe the formation of homogeneous and extended lamellae as well.

1. Introduction

Whenever the crystallization of polymers shall be investigated in situ by means of scattering methods, the information content of the scattering pattern can be increased significantly by studying a material which crystallizes in the uniaxially oriented state instead of studying an isotropic sample. Oriented crystallization of polymers can be achieved by several techniques. As we are cautiously melting highly oriented materials with fiber symmetry in order to preserve the orientation memory of the polymer network, other scientific groups induce highly oriented crystallization by shearing a melt.[1−7]

A great advantage of shear-induced crystallization experiments is the fact that one can easily start from an equilibrated melt. Memory effects with respect to the material's initial nanostructure before melting can easily be minimized. When, on the other hand, anisotropy is based on preservation of orientation memory in the melt, it may happen that crystals or nuclei have been left over, and the original nanostructure of the sample is at least partially restored. Nevertheless, the oriented crystallization from a quiescent polymer melt is beneficial in other respects: during the experiment no mechanical stress is put on the sample.

The isotropic crystallization of polypropylene has been studied for decades. Whenever early studies are focusing on the evolution of the nanodomain topology they are, in general, employing the transmission electron microscopic (TEM) survey of samples that have been quenched during crystallization and stained. Thus, Norton and Keller[8] discover a peculiar topology in polypropylene, the so-called cross-hatched structure. Later this topology is verified and studied in detail by other authors.[2,9,10] According to Olley and Bassett,[9] the cross-hatched structure is only formed during secondary crystallization. According to their studies, primary crystallization is governed by growth of common lamellae that are rarely interconnected. However, small-angle X-ray scattering (SAXS) has frequently been employed as well—in particular, for in-situ studies of structure evolution in isotropic polypropylene. The data from most of these SAXS studies are collected using a setup that is integrating over a big irradiated volume. This means that the coupling of data to the domain topology is weaker when the SAXS method is employed than it is when the material is studied by TEM. Therefore, SAXS investigations of isotropic material are frequently coupled with other methods. The group of Hsiao[11] studies well-defined fractions of polypropylene which are free of nucleating agents and finds that the crystallization closely follows the classical mechanism of nucleation and growth. A similar finding is reported by the group of Cebe.[12,13] On the other hand, the group of Ryan[14,15] is studying commercial polypropylene and finds that the formation of crystals is preceded by a phase separation. According to their results, the crystallization is a multistage process that starts from a mesophase. Strobl[16,17] extracts a similar but even more detailed result. According to the Strobl mechanism, the disentangled mesophase is, first, seeded by assemblies of blocks which, second, fuse to become lamellae.

Modern microbeam SAXS equipment even permits to study the local anisotropic structure inside a globally isotropic material. Thus, the common disadvantage of averaging over a big irradiated volume can be circumvented. If the microbeam is

† Dedicated to Prof. Dr. S. Fakirov on the occasion of his 70th birthday.
‡ University of Hamburg.
§ HASYLAB at DESY.
⊥ ESRF.
* Corresponding author: e-mail norbert.stribeck@desy.de; Tel +49-40-42838-3615; Fax +49-40-42838-6008.

10.1021/ma070251t CCC: $37.00
Published on Web 05/26/2007

monitoring a small spot in the polypropylene melt during a crystallization experiment, the growth of nanostructure after passing of the spherulite growth front can be documented in time-resolved anisotropic two-dimensional (2D) SAXS patterns. Application to polypropylene crystallization at low undercooling (i.e., shallow quench) from the melt shows that the main mechanism of secondary crystallization is the growth of lamellar crystallites in remnant amorphous regions.[18]

As here we study crystallization in a macroscopically oriented material, we are not the first who exploit the orientation memory in a melt of polypropylene. Several studies[19−23] are dealing with orientation memory and report that, in general, the residual structure substance is a melt orientation of the polymer chains in polypropylene which only vanishes at elevated melt temperature. However, there may even be other carriers of orientation memory, particularly in polypropylene. The reason is that most commercial polypropylene grades are containing smart additives (clarifiers, nucleating agents)[5,24,25] that control the formation of nanostructure. In this case the typical needle-shaped moieties assembled in the melt from such additive molecules[7] may be the carriers of orientation memory. By means of these agents, the final product may be clarified, a preferential crystal modification may be chosen, and the considerable undercooling required for the crystallization of pure polypropylene is reduced. As a result, the technical PP grade is already crystallizing at a higher temperature than the typical 110 °C,[7] which are required for pure PP under production conditions.

In this study we encounter a peculiar SAXS pattern with fiber symmetry, which can be explained both by Keller's cross-hatched structure and by Strobl's block structure because of the ambiguity inherent to Babinet's theorem. On the other hand, if crystallization from a quiescent melt is studied in a time-resolved experiment, the evolution of the anisotropic scattering pattern provides additional information on the structure evolution mechanism that can help to discriminate between the two models.

According to conference contributions presented by several groups during the year 2006, evolution of the same pattern is observed during shear-induced crystallization of polypropylene. In order to describe the observed evolution, we have heard the tentative interpretation that a cross-hatched structure is formed very fast and the connecting "daughter lamellae" are disrupted from shear force, finally resulting in a lamellar system. It is the intention of this paper to demonstrate why it appears to us that a block-structure mechanism is the more probable one.

2. Experimental Section

Materials. Commercial hard-elastic[26,27] polypropylene (PP) film (CelGard-PP, Lot #884, as extruded by Hoechst-Celanese) of 25 μm thickness is studied. The films are produced[28] from the PP grade Hercules Profax 6301 with a melt index 15.0 (230 °C) ASTM-D-1238. The weight-average molecular mass of the grade is $\bar{M}_w$ = 128 000 g/mol. The polydispersity of the material is $\bar{M}_w/\bar{M}_n = 4$. Sixteen sheets are stacked under consideration of their high uniaxial orientation, covered by aluminum foil (20 μm thickness), and fixed in a frame.

SAXS Measurements. Small-angle X-ray scattering (SAXS) is performed in the synchrotron beamline BW4 at HASYLAB, Hamburg, Germany. The wavelength of the X-ray beam is 0.1366 nm, and the sample−detector distance is 13 155 mm. Scattering patterns are collected by a two-dimensional position-sensitive marccd 165 detector (mar research, Norderstedt, Germany) in binned 1024 × 1024 pixel mode (158.3 μm quadratic pixel size). Scattering patterns are recorded every 30 s with an exposure of 28 s. The oriented SAXS pattern of the untreated hard-elastic material is published in the literature.[28−30] It shows very narrow meridional scattering with the first and second order of the long period reflection clearly visible.

High-Brilliance Beam Melts Polypropylene. It appears worth mentioning that we have, as well, unsuccessfully tried to perform simultaneous small-angle and wide-angle X-ray scattering (SAXS/WAXS) measurements with high cycle time during polypropylene crystallization at beamline ID2 of the ESRF in Grenoble. The main problem has been that the high-brilliance synchrotron beam of ID2 has acted as a second heater, having molten the polypropylene sample in the irradiated volume completely as soon as the temperature of the furnace has exceeded 166 °C. This problem may as well be specific to the polypropylene grade or to the specific geometry (sample made from 16 thin sheets instead of a single piece of polymer) because we did not experience similar problems in previous studies of polyethylene rod-shaped material.[31] As a result, the patterns recorded at ID2 were not reproducible. They did not show point symmetry but long streaks under varying oblique angle, or the patterns were isotropic. It appears worth mentioning this failure because we have to report the reason for the fact that we have so little information on the wide-angle X-ray scattering and on the evolution of the crystallization on a short time scale.

In order to overcome the experienced shortcoming, one would have to change the oven experiment for use at a high-brilliance beamline considerably. If one would do without high time resolution, one could choose to flash short pulses of light on the sample and wait in darkness, until the heat pulse has been dissipated across the sample. If high time resolution is required, one could choose to spread the heat exposure by continuously moving the sample in the beam.

Temperature Programs. The frames containing each a stack of foils are mounted in a furnace equipped with two heating cartridges and air cooling that is provided at the beamline. The samples are rapidly heated to 150 °C. Then the heating rate is lowered to 2 °C/min in order to cautiously approach a melt-annealing temperature which is chosen between 168 and 178 °C. The melt-annealing temperature is kept for 4 min. After this time differing cooling programs are performed. In the case of isothermal crystallization experiments, the sample is cooled to the crystallization temperature with a heating rate of −2 °C/min in order to avoid overshooting. The isothermal phase is between 30 and 35 min. In addition, nonisothermal crystallization experiments during rapid quench (initial cooling rate[63] >100 °C/min) are carried out. During the temperature treatment SAXS patterns are continuously recorded in order to identify mechanisms of melting and crystallization.

List of Experiments Carried Out. In order to identify the melt-annealing temperature above which no oriented recrystallization is obtained, first different melt-annealing temperatures are tested. Thereafter isothermal crystallization experiments at 150 °C are carried out after melt-annealing at 168, 170, 171, 174, 175, 176, and 178 °C. Moreover, for one of the melt-annealing temperatures (171 °C) three additional crystallization temperatures (140, 145, and 155 °C) for isothermal experiments are chosen. The nonisothermal rapid quench experiment has started from a melt-annealing temperature of 171 °C as well.

SAXS Data Evaluation. Data analysis of the SAXS data is carried out by means of the multidimensional chord distribution function (CDF) method. This method has been developed and published 7 years ago.[32] Its application has repeatedly been described in detail in many of our earlier papers (cf. refs 33−40). Moreover, it is exemplified in a textbook (Stribeck,[41] section 8.5.5). For a schematic sketch of the steps of data analysis and the extraction of structural parameters from the CDF, see for example Figure 2 in Stribeck et al.[42] and the example at the end of this paragraph. The analysis is carried out using computer programs developed under Linux and pv-wave[43] in order to extract information on nanostructure (i.e., a two-phase topology, $\rho(r) \in [\rho_{cryst}, \rho_{amorph}]$, of phases with distinct densities) from two-dimensional (2D) SAXS patterns. The result is an "edge-enhanced autocorrelation function", $z(\mathbf{r})$—the autocorrelation of the gradient field, $\nabla\rho(\mathbf{r})$. Thus, as a function of ghost displacement, $\mathbf{r}$, the multidimensional CDF $z(\mathbf{r})$ shows peaks wherever there are domain surface

contacts between domains in $\rho(\mathbf{r})$ and in its displaced ghost. It visualizes size and arrangement of the nanodomains in the sample, e.g., long period, lamella thickness, and extension. The CDF with fiber symmetry in real space, $z(r_{12},r_3)$, is computed from the fiber-symmetrical SAXS pattern, $I(s_{12},s_3)$, of multiphase materials with uniaxial orientation.[32] $\mathbf{s} = (s_{12}, s_3)$ is the scattering vector with its modulus defined by $|\mathbf{s}| = s = (2/\lambda) \sin \theta$. Here λ is the wavelength of radiation and 2θ is the scattering angle. No model is required to compute the CDF. Apart from uniaxial symmetry it is only assumed that the nanostructure is sufficiently imperfect. In the historical context the CDF is an extension to Ruland's interface distribution function (IDF)[44] to the multidimensional case or, in a different view, the Laplacian of Vonk's multidimensional correlation function.[45]

In practice, a simple estimate for the lateral extension, L_e, of the crystalline lamellae is obtained from the base width of the layer correlation triangle in Figure 1a. A most probable long period, L (cf. Figure 1b), is obtained from the distance in meridional direction between the first-order long-period peaks of the CDF. In the beginning of crystallization the CDF shows more features (cf. Figure 6).

Machine background weighted by the absorption factor is subtracted from the raw data. Invalid pixels (e.g., beam stop) are discarded by masking. The image is aligned, rotated, harmonized (assuming fiber symmetry), and extrapolated both into the remnant beam stop area and toward high scattering vector. The multidimensional extrapolations are carried out by means of the radial basis functions. [43,46] The data preevaluation is described in a textbook.[41] Thereafter, the data are projected on the fiber plane amd multiplied by s^2 (Laplacian in real space), the background due to the nonideal nature of the two-phase system is removed by spatial frequency filtering, and an interference function, $G(\mathbf{s})$, is obtained. From $G(\mathbf{s})$ the CDF $z(\mathbf{r})$ is computed by Fourier transformation.[32]

3. Results and Discussion

3.1. Melting of the Highly Oriented Material. Figure 2 shows SAXS patterns taken during the heating of the hard-elastic PP precursor material. The images from the temperature range between 152 and 164 °C demonstrate the high uniaxial orientation of the material. The characteristic feature of the pattern is represented by the two long-period reflections on the meridian (s_3-direction in reciprocal space).

Figure 3 shows the melting of the precursor hard-elastic polypropylene material in the view of the CDF, $z(r_{12},r_3)$. In the top row we observe many horizontal streaks with alternating positive and negative sign which, in the pseudo-color images $|z(r_{12},r_3)|$, are all mapped to positive values. By counting the number of visible streaks with negative sign (i.e., the long-period streaks), we estimate that even at these high temperatures the correlation among the crystalline layers is extending up to the third neighbor. Moreover, the horizontal streaks of lamellae and long periods do not show modulation at any time of the melting process. Thus, the lamellae are continuously melting down from their surface—there is no disintegration of lamellae into blocky domains while the hard-elastic material is heated. In the lower row of Figure 3 the chosen melt-annealing temperature of 171 °C has been reached, the first image being taken 4 min before quenching to crystallization temperature. We observe a broad distribution of thick and short lamellae with little correlation among them in fiber direction. The middle image in the bottom row clearly shows a row assembly of nuclei extending along the fiber direction. This structure is observed in three successive images, until 2 min before quenching (cf. image in the bottom left corner of Figure 3) even the row structure is almost completely gone. Now the material is molten.

Figure 4 shows the evolution of nanostructure parameters as measured during the heating of the hard-elastic PP material. Open circles show the long period as determined directly from the position of the peak maximum in the measured SAXS pattern. CDF data are missing for temperatures below 152 °C because the discrete SAXS does not completely fit into the detector area at such low temperatures, and therefore a CDF cannot be computed. Above 170 °C the material shows little or no discrete SAXS anymore.

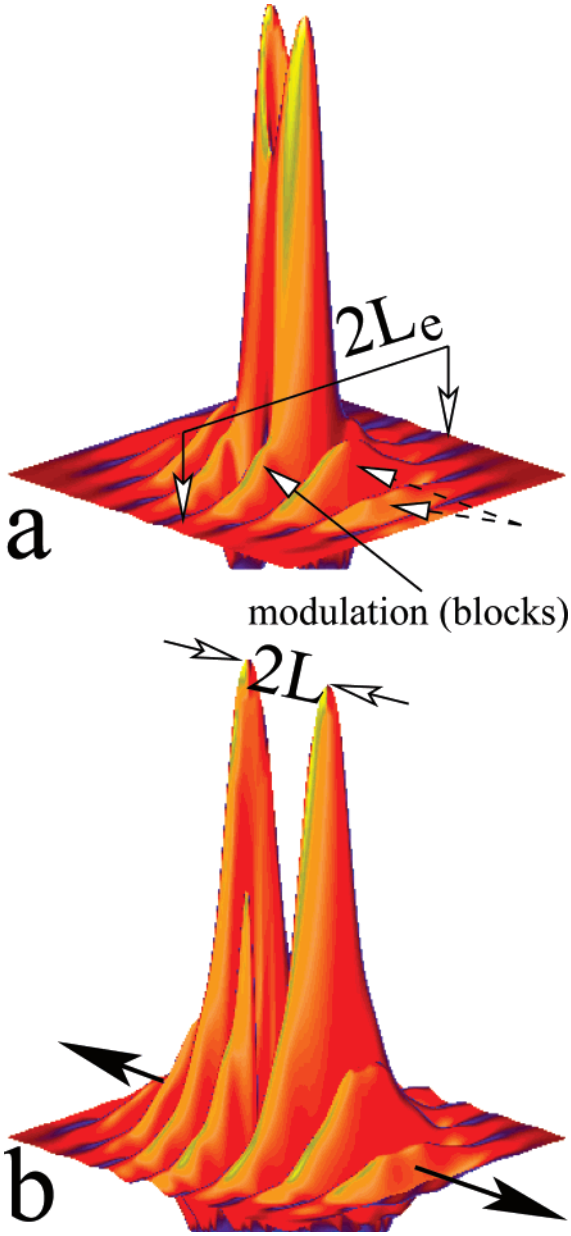

Figure 1. Demonstration of CDF analysis for the simple case of a predominant lamellar system (melting PP; the function is shown in an interval -100 nm $< r_{12}, r_3 <$ 100 nm). (a) shows the positive face, $z(\mathbf{r})$, with the layer peaks visible. $2L_e$ is the double lateral extension of a single layer. The solid-line arrow indicates a modulation inside the lamella in lateral direction which is typical for a blocky system. The sandwiches of two or three lamellea (broken-line arrows) are not modulated. (b) shows the negative face, $-z(\mathbf{r})$, with the long-period peaks visible. The distance between the two small arrows on top is the double long period. The filled arrows below indicate the fiber direction, r_3.

The figure shows that with such a highly oriented material the long period can perfectly be determined from the scattering pattern. The more involved CDF method returns the same values. Between 150 and 160 °C we observe a small but continuous increase of the long period that is followed by a plateau. A second increase of L is found above 165 °C.

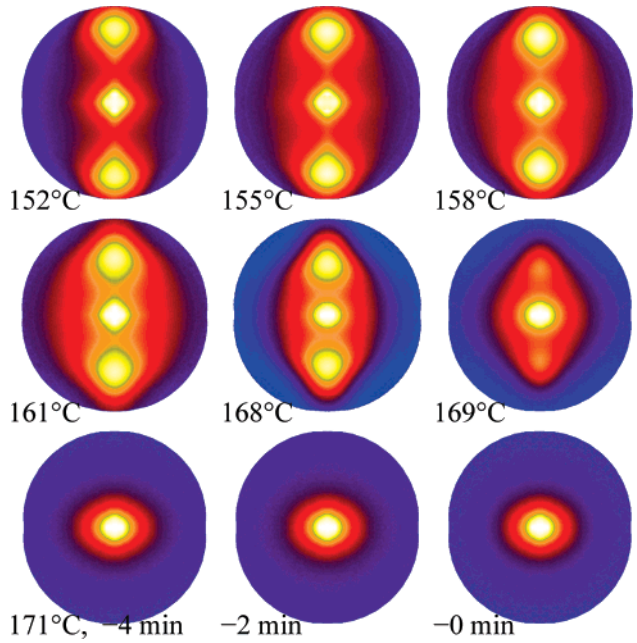

Figure 2. SAXS patterns recorded during the heating and melting of PP (logarithmic intensity scale). Sample temperatures and times before quench to crystallization temperature are indicated. The sensitive region is 0.002 $nm^{-1} < |\mathbf{s}| < 0.05\ nm^{-1}$ in reciprocal space. s_3-direction (i.e., orientation axis, fiber axis, meridian) is vertical.

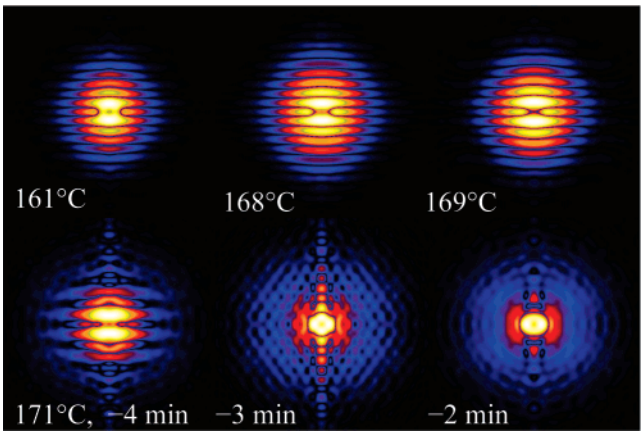

Figure 3. Nanostructure in real space ($|z(r_{12},r_3)|$, i.e., absolute values of CDFs) during the heating and melting of hard-elastic PP. Sample temperatures and times before the quench are indicated. The images show the region $-150\ nm < r_{12}, r_3 < 150\ nm$ in real space. r_3-direction (i.e., orientation axis or "fiber" direction) is vertical.

The lateral extension of the lamellae can only be determined from the CDF. As a function of temperature the measured data do not show a monotonous trend. This finding indicates that the melting process of the hard-elastic material is not governed by a single mechanism. The observation can be explained if we assume that two kinds of crystalline lamellae (e.g., primary and secondary ones) with different melting behavior are present.

Melting Mechanisms. Describing the melting process under this premise, we first observe the melting of less-extended secondary lamellae up to a temperature of 158 °C. On one hand, this mechanism generates the observed significant increase of the average lateral extension of the remnant lamellae. On the other hand, it goes along with an only slight increase of the overall long period.

In the temperature interval between 158 and 162 °C another mechanism is predominating. In this interval we observe both a considerable decrease of the average lateral extension of the lamellae and an increase of the average long period. The mechanism may be interpreted as the melting of extended secondary lamellae.

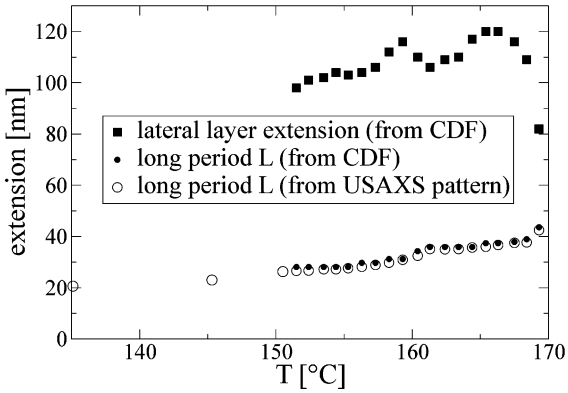

Figure 4. Evolution of nanostructure parameters in hard-elastic PP during heating to the melt. Heating rates: 2 °C/min above 150 °C; 20 °C/min below 150 °C.

The third mechanism is similar to the first one. Between 162 and 165 °C, the long period remains almost constant and the average layer extension is increasing, indicating the melting of (now the primary) crystalline lamellae with the less extended layers melting first.

Finally, in a fourth regime, above 165 °C a steep decrease of the average layer extension is observed. It can be explained by the melting of even the last and widely extended primary lamellae. The bottom left CDF in Figure 3 shows that the lamellae melt down from their surface and do not disintegrate into blocks during this process.

3.2. The Oriented Melt. The SAXS pattern and the CDF do not show significant discrete nanostructure if a melt-annealing temperature of at least 170 °C is kept for 4 min. This means that, in general, under this condition the material has been molten completely.

Subsequently, the melt is found to crystallize with high uniaxial orientation again, as long as the melt-annealing temperature has not exceeded 177 °C.

After raising the melt-annealing temperature above 177 °C, the sample always starts to crystallize isotropically from the very beginning. This means that in this case the orientation memory has been erased. Thus, for the studied PP the melt-annealing temperature window for an anisotropic, quiescent crystallization is 6 °C wide. This window is wider than with the polyethylene grades previously studied[40,47,48] where the corresponding width was only 2 °C. A possible reason for this wide anisotropic crystallization window may be the fact that the orientation information on commercial PP grades is most probably stored not only in the entanglement network (i.e., taut, disentangled chain segments extending between highly entangled knots)[23] but also in elongated assemblies built from molecules of added nucleating agents.[7]

A variation of the melt-annealing temperature within the anisotropic crystallization interval has little effect on the evolution of nanostructure. The main observed effect is a higher probability of incomplete melting, if the temperature is adjusted close to the lower end of the interval.

3.3. Nanostructure Evolution and Cooling. In this section we report on the observed nanostructure evolution in our anisotropic material as a function of a chosen isothermal crystallization temperature. Studies on isotropic quiescent crystallization of polypropylene with a focus on this chosen

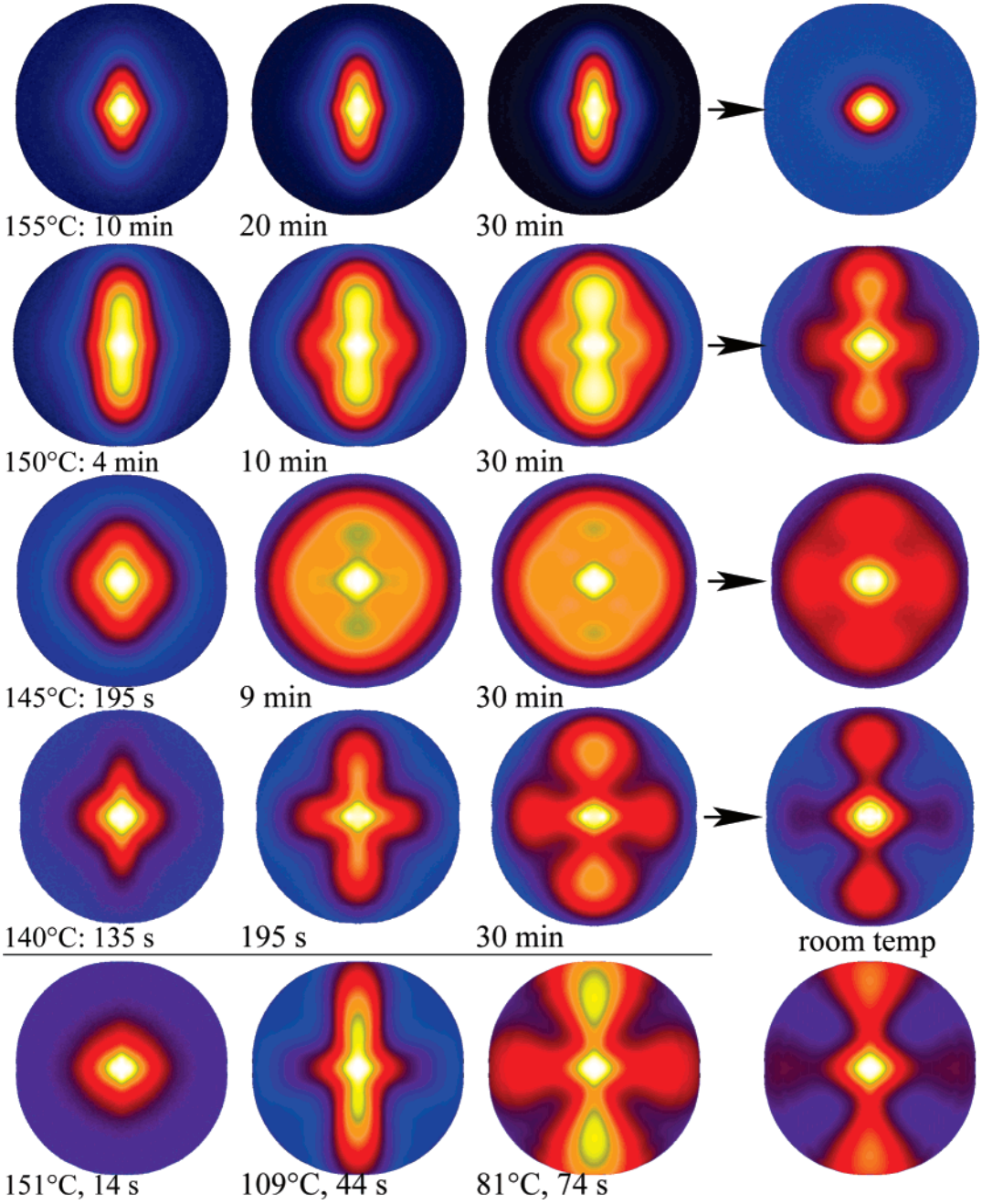

Figure 5. Oriented quiescent crystallization of PP from a melt of 171 °C quenched to different crystallization temperatures as a function of time. Pseudo-color images of the measured SAXS patterns (logarithmic intensity scale). The rightmost column shows the ultimate nanostructure after cooling to room temperature. Bottom row: nonisothermal crystallization (rapid direct quench).

undercooling by means of X-ray scattering have been carried out by the groups of Ryan[15] and Hsiao.[49]

Figure 5 presents typical scattering patterns observed as a function of time and crystallization temperature. The bottom row shows data accumulated during nonisothermal crystallization in a steep temperature gradient (−100 °C/min).

3.3.1. Crystallization at 155 °C. Stochastic Anisotropic Lamellae Growth. At the highest crystallization temperature studied (155 °C) it takes several minutes before discrete SAXS is observed. In the top row of Figure 5 scattering patterns are shown, which have been recorded after 10, 20, and 30 min. The length of a meridional streak is growing. This phenomenon has as well been observed in preceding studies during the crystallization of polyethylene. By means of quantitative CDF analysis, it has been identified as evolution of the random nanostructure of uncorrelated crystalline lamellae,[50] a phenomenon that in polymer science has first been described by Schultz et al.[51] In mathematics the corresponding mechanism is called a "random car parking process";[52,53] one of the mechanisms studied in the field of random sequential adsorption.[54] During the isothermal period of 30 min no intensity maximum is growing from the streak. This means that even after 30 min the volume is still sparsely populated with lamellae. The population density is far below the so-called jamming limit.[52]

For polypropylene a crystallization temperature of 155 °C is a shallow quench. Our data taken during the first 30 min are not in contradiction to the classical nucleation-and-growth[55] model of crystalline lamellae because there is no clear indication that a blocky mesostructure according to Strobl's mechanism[16] is preceding the formation of lamellae. On the other hand, the simple SAXS experiment cannot detect a mesostructure with domains of lamellar shape. A suitable experiment that may

reveal a lamellar mesophase is a simultaneous SAXS/WAXS experiment with high cycle time, as it has been carried out frequently for isotropic material[11,15] and even for highly oriented polyethylene.[31] As stated above, we have carried out similar measurements with our polypropylene but were unsuccessful because of uncontrollable sample heating by the brilliant synchrotron beam itself.

Stochastic−Isotropic Crystallization. After 30 min the material is cooled to room temperature at a cooling rate of 20 °C/min. The scattering pattern to the right of the horizontal arrow represents the ultimate structure of the sample. We observe only diffuse and isotropic SAXS, as is typical for isotropic and random placement of (the secondary) crystallites. The images taken continuously during cooling show that this stochastic−isotropic crystallization is starting, as soon as the temperature drops below 110 °C. Such a stochastic−isotropic crystallization upon cooling has been observed in several of our experiments. For the melt-annealing temperature of 171 °C it is only observed for the highest studied crystallization temperature (155 °C). Beginning with a melt-annealing temperature of 174 °C it is, as well, observed for the crystallization temperature of 150 °C.

3.3.2. Crystallization at 150 °C. Stochastic Anisotropic Lamellae Growth. At 150 °C the crystallization is considerably faster than at 155 °C (see Figure 5). Already after 4 min the meridional streak is stronger than after 30 min in the shallow quench experiment. Thus, the evolution of the scattering pattern during the time-resolved experiment shows that the primary mechanism, again, is that of building homogeneous lamellae.

Evolution of Laterally Structured Assemblies. After 7 min at 155 °C a streak on the equator begins to grow longer and longer. After 10 min (see Figure 5, second row) it has already started to turn the meridional streak into a cross-pattern. A second crystallization mechanism has begun. As after 30 min the chosen isothermal period is almost over, the equatorial streak has grown noticeably. Moreover, it is also present in the cooled material at room temperature. Anticipating the CDF analysis presented beneath, this pattern indicates the scattering of laterally nanostructured assemblies and can be explained both by Strobl's block structure and by Keller's cross-hatched structure in a highly oriented material. It is the block structure, if this lateral modulation of density is impressed on the crystalline phase. On the other hand, the lateral structure may as well be impressed on the amorphous layers. In this case neighboring crystalline layers must be interconnected by crystalline struts or daughter lamellae, and this is the cross-hatched structure. On the basis of the data of this experiment, they can hardly be discriminated from each other.

3.3.3. Crystallization at 145 and 140 °C. Evolution of Laterally Structured Assemblies. With increasing undercooling the crystallization is not only accelerating more and more but also is the formation of a pure meridional streak no longer detectable. Already the first SAXS pattern with discrete scattering is a cross-pattern (see Figure 5, third and fourth rows).

Transformation of Laterally Structured Assemblies into Lamellae. As the crystallization is advancing the scattering intensity in the (vertical) meridional streak is increasing, whereas the equatorial scattering is decreasing. Thus, we observe a transformation from laterally nanostructured material into lamellae.

Because of the fact that our crystallization experiment is carried out isothermally from a quiescent melt, it can hardly be assumed that we are observing crystalline cross-hatched daughter lamellae[2] or struts during melting or rupture (e.g., by shear force). On the other hand, our results are in perfect agreement with the crystallization mechanism of "building lamellae from blocks", as developed by Strobl.[16,17] According to this mechanism assemblies of blocks are fused into homogeneous crystalline lamellae. Discrete equatorial scattering is reduced in favor of discrete meridional SAXS.

3.3.4. Nonisothermal Crystallization. The bottom row of Figure 5 displays scattering data accumulated during nonisothermal crystallization, i.e., rapid quench from the melt-annealing temperature of 171 °C with an initial cooling rate of about 100 °C/min. Each pattern is labeled both with the time after quench and the average temperature during exposure. Exposed to the steep temperature gradient, the first image with discrete SAXS shows the very long meridional streak of an oriented ensemble of (primary) lamellae with random placement of the domains, as is confirmed by CDF evaluation and its results in analogy to published work on polyethylene.[40,56] Only weak equatorial scattering is present. Already the next pattern taken after 74 s shows the effect of inserted secondary lamellae (long period maxima at the meridian due to placement in the centers of the remnant gaps[18,50]). The inner "blocky texture" of secondary lamellae is demonstrated by the strong equatorial streak.

Compared to the isothermally crystallized material, nonisothermally crystallized polypropylene shows scattering patterns which cover a much wider range in reciprocal space. In this respect they are comparable to the patterns of the hard-elastic precursor material at low temperature with its low long period. For in-depth studies of both materials with a nonisothermal history it would be necessary to shorten the distance between sample and detector considerably.

3.4. CDF Analysis of the SAXS Cross-Pattern. Figure 6 shows the CDF computed from the SAXS pattern in the lower left corner of Figure 5. Because of the fact that crystallization has just started, the corresponding CDF does not yet show any smearing due to a superposition of early and late scattering entities. Figure 6a shows the peaks of the CDF which carry a positive sign. The distances of the peak maxima from the center of the CDF pattern, $z(r_{12},r_3)$, are measures for the distances between a "beginning" and an "end" of domains. The peaks are labeled by letters d, e, f, g, h, and i. In Figure $6c_1$ the corresponding distances are indicated by solid arrows.

Figure 6b shows the negative peaks of the CDF. The distances of the peak maxima from the center of the CDF pattern are measures for the distances between "beginnings" (or "ends") of correlated domains. In Figure $6c_1$ the corresponding distances (k, l, m, n, o, p) are indicated by broken arrows.

Figure $6c_1$ presents a sketch of the block model derived from the CDF. It shows average sizes and arrangement of the blocks in the orientation direction (r_3) and in the transverse direction (r_{12}) of the material, respectively. According to Babinet's theorem, phase inversion of the structure does not change the scattering pattern. Thus, also the phase-inverted structure in Figure $6c_2$ explains the static SAXS pattern. Obviously, this is the image of a cross-hatched structure.

Block Structure Evolution at 140 °C. Figure 7 shows the evolution of the block structure during the crystallization experiment at 140 °C. Variation is only observed during the first 3 min. During this period the temperature is still decreasing from the melt-annealing level (171 °C). At the beginning of the true isothermal interval, the 3D arrangement of the blocks changes from an entwined one (see Figure 6 and left inset in Figure 7) to a straight one (right inset in Figure 7). The sketches in the insets are highly idealized. In reality, there is only short-range correlation among neighboring blocks, no lattice.

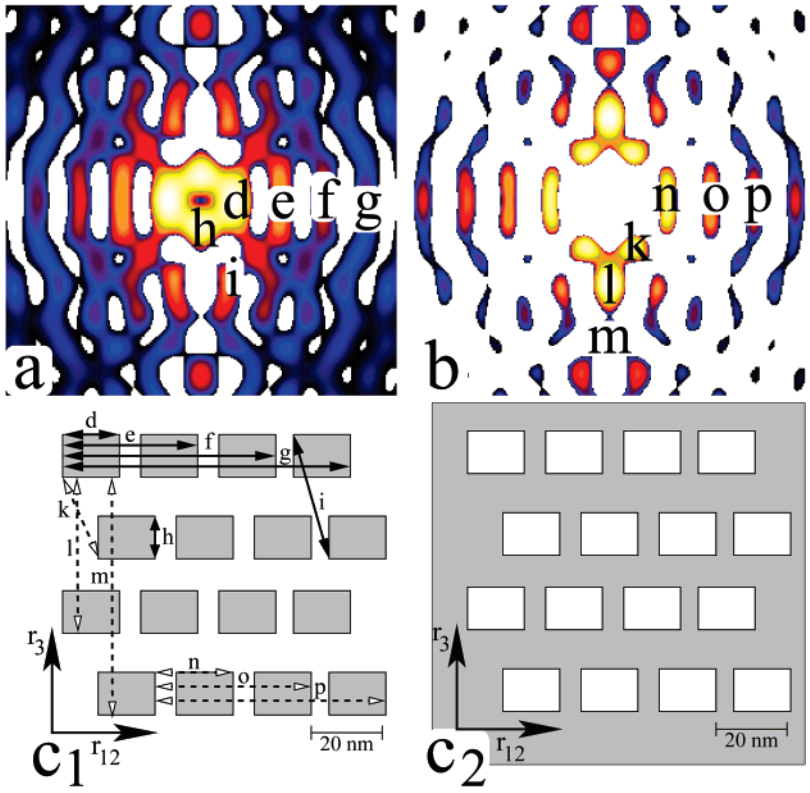

Figure 6. CDF computed from a SAXS cross-pattern for the purpose of nanostructure analysis: (a) positive peaks (domain sizes); (b) negative peaks (long periods); (c_1) block-structure model with block sizes and distances as read from the positions of the CDF peaks; (c_2) the cross-hatched model obtained by phase inversion of the block-structure model.

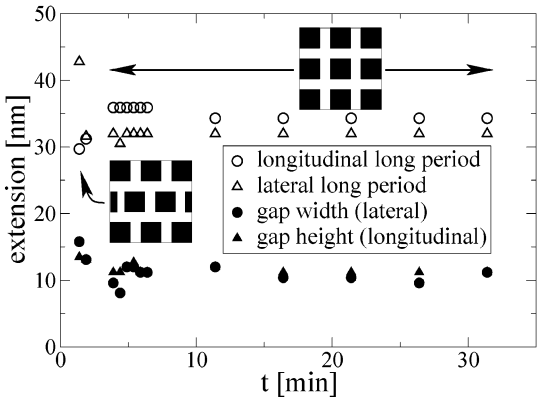

Figure 7. Evolution of the block nanostructure during crystallization at 140 °C. Two observed block arrangements are sketched in insets. During the first 3 min the temperature is not yet constant, and the block arrangement (left inset) is different from the arrangement (right inset) during the isothermal period.

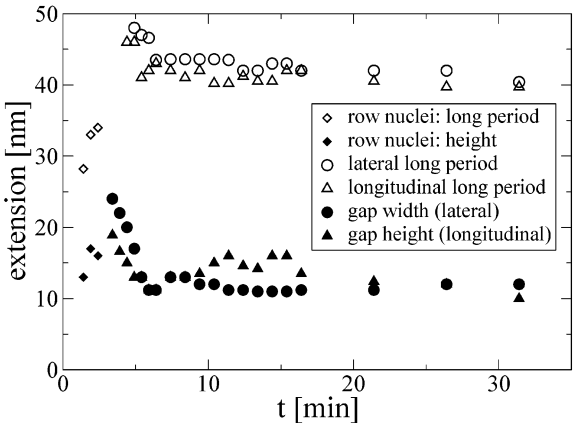

Figure 8. Evolution of the nanostructure during crystallization at 145 °C. During the initial nonisothermal phase row nuclei (diamonds) show up first. After 3 min they are replaced by a block structure.

During the truly isothermal period of the experiment the scattering pattern (see Figure 5, fourth row) is changing. We observe a relative increase of the meridional scattering of the lamellae with respect to the equatorial scattering. It thus can be assumed that the constant block size from the CDF analysis indicates a dynamic equilibrium, and the observed nanostructure describes the average block structure of a system in which local assemblies of blocks are emerging, ripening, and fusing to become lamellae.

Nanostructure Evolution at 145 °C. Figure 8 demonstrates the evolution of the nanostructure at 145 °C as extracted from the CDF. We have to point out that we cannot analyze the weaker lamellar system, and our very simple analysis of the block system assumes that the influence of the lamellar system is negligible. For the experiment presented here this assumption appears only to be a very coarse approximation. During the first 3 min after the quenching the experiment is nonisothermal. In this interval we observe only a row assembly of nuclei, i.e., tiny domains with longitudinal arrangement. Thereafter, we observe a block structure (lateral arrangement of blocky domains). Two CDFs from the isothermal phase are shown in Figure 9. 4.5 min after quenching (Figure 9a,b) the individual blocks are still rather uniform, the long period peak (Figure 9b) is still restricted to the width of the row of blocks, and there is still some midrange correlation among the domains. Thereafter, the nearest-neighbor correlations among the blocks are growing on the expense of longer ranging correlations. Figure 9d shows broad triangular long period peaks which are typical for domains of lamellar shape. The lateral long period (open circles) is resulting from the gaps in the blocky layer, which has narrowed between 4.5 and 9 min after quenching (cf. Figure

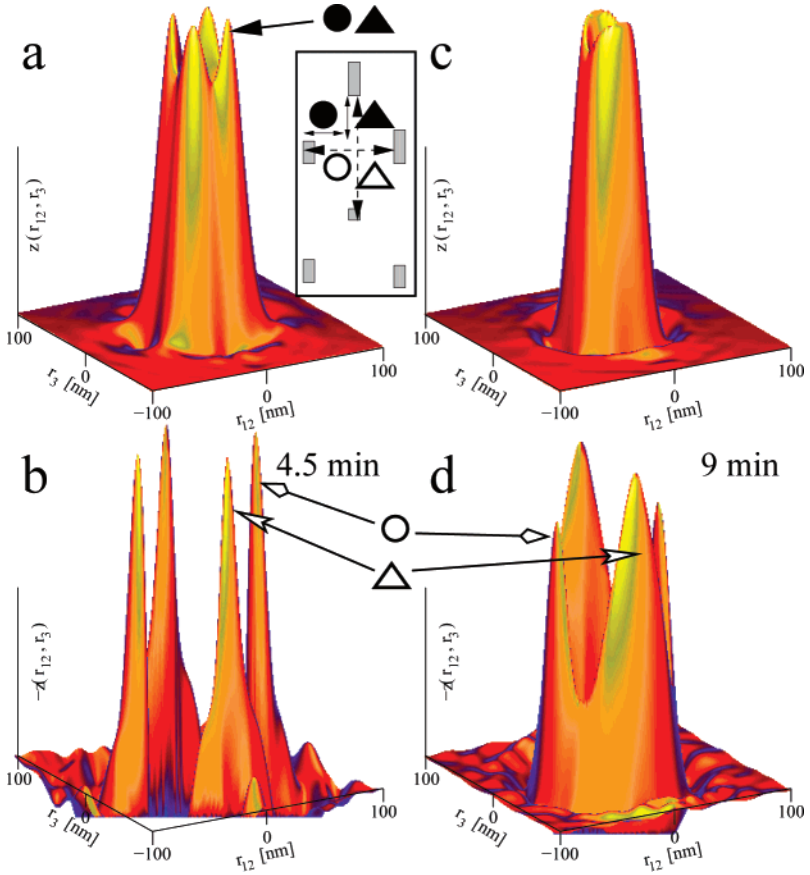

Figure 9. CDFs during the isothermal phase of PP recrystallization at 145 °C: top, positive faces; bottom, negative faces. After 4.5 min (a, b) the initial short-range correlated block structure (cf. Figure 6) is still visible. Arrows point at the peaks of the CDF. The indicated symbols are related to the curves shown in Figure 8. The inset shows the relation of the quantities to the simple nanostructure model. After 9 min (d) in the shortest-range correlations between neighboring domains have considerably widened.

8). During the following 20 min of the isothermal period the principal character of the CDFs does not change any more. The prominent domain peaks are formed by the (amorphous) gaps between the blocks. The size distribution of the blocks themselves is broad, and determination of its maximum would require separation of the components by fitting to a multicomponent topological model.

In the interval between 10 and 15 min Figure 8 exhibits a faint effect that might be related to an interesting mechanism. The triangle symbols show an increase of the amorphous gap "in chain direction", while at the same time the height of the crystalline block is decreasing. This observation could be related to a purification process in which disorder is moved out of the crystal along the chain direction.

Nanostructure Evolution at 150 °C. Quenched to this crystallization temperature, the melt is starting to produce lamellae from the very beginning. The block structure is still visible in the scattering pattern, but in the CDF it is very weak and cannot be analyzed as long as the lamellar structure cannot be separated. Figure 10 demonstrates the evolution both of the long period and of the average layer thickness as extracted from the position of the broad domain peak maximum in the CDF. At the time when the first lamellae are observed in the CDF, the crystallization temperature has not yet been reached. Thereafter, the open triangles show a strongly decreasing long period during the first 6 min. In analogy to the analyses of similar CDFs in our previous studies,[23,40,48,50] we attribute this effect to volume filling by the random car parking process.[52,54] The following slow decrease of average long period and layer thickness can be explained by an insertion of blocky lamellae

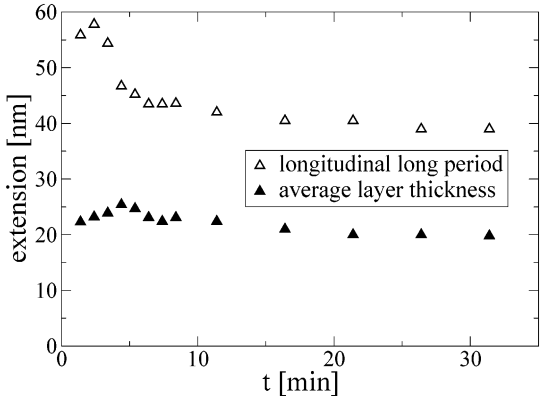

Figure 10. Evolution of the nanostructure during crystallization at 150 °C. Lamellae are observed from the beginning of structure formation. Amorphous and crystalline thickness are merged into one broad peak. Filled triangles show the evolution of the position of its maximum.

which show up in the measured equatorial scattering (see Figure 5, second row).

Compared to the crystallization at 150 °C, the crystallization experiment at 155 °C shows similar behavior at a considerably reduced crystallization speed.

3.5. Remelting the Incompletely Fused Lamellae. Figures 2 and 3 show the melting of the original hard-elastic PP material—a nanostructure built from homogeneous crystalline lamellae that are continuously melting down from their surface. This structure has been formed by nonisothermal crystallization under extreme gradients of temperature and pressure.[26,57,58] In contrast, the result of the isothermal oriented recrystallization

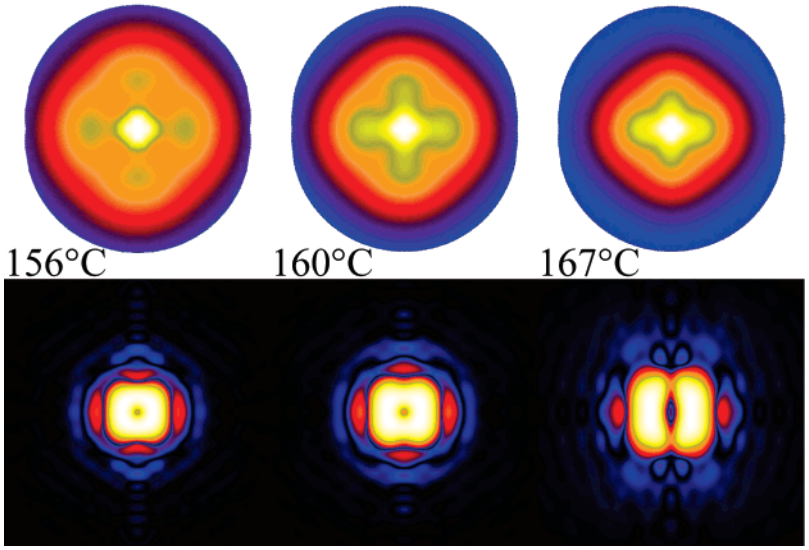

Figure 11. Second melting of PP material previously crystallized at 140 °C. Top row: SAXS patterns. Bottom row: CDFs $|z(r_{12},r_3)|$. The regions shown are the same as in the corresponding previous figures.

from the quiescent melt at high undercooling is no perfect layer system.

As revealed in Figure 5, we ultimately end up with a nanostructure which can be explained with the block model. Here each crystalline lamella resembles a bar of chocolate crossed by break lines. If this hypothetic structure is a good approximation of reality, we can test it in a remelting experiment in order to gain more evidence.

During such a remelting experiment each scattering pattern should differ in a characteristic way from the scattering patterns observed during crystallization, if the block model is valid. This can be explained as follows: In the chocolate bar layer topology the majority of the lamellae carry break lines. Such lamellae should not continuously melt down but should decompose into blocks, before the individual blocks themselves melt down. In this case the meridional "lamella intensity" should feed the equatorial "block intensity", while both are vanishing. Thus, during remelting the equatorial streak should be stronger than the meridional one because it is continuously fed from the decomposing lamellae. Such equator-accentuated patterns would be just the contrary of the meridian-accentuated patterns observed during the isothermal crystallization.

On the other hand, if the remelting nanodomain topology were a cross-hatched structure, the less stable "daughter lamellae" should melt down before the extended primary lamellae. In this case the equatorial scattering would always be weaker than the meridional streak, and even during remelting the patterns would be meridian-accentuated in a similar manner as during the isothermal crystallization experiments.

As a result of a lucky operator error we unintentionally recorded a series of SAXS patterns during remelting after the experiment which resulted in the ultimate scattering pattern shown in the lower right corner of Figure 5. Because we forgot to replace the sample, we now have good time-resolved remelting data of this sample for temperatures above 155 °C.

Figure 11shows three stages of the evolution. As expected for a metastable block structure, all the scattering patterns here appear equator-accentuated. Even the images of the absolute CDF shown in the row below exhibit the strongest correlations in the horizontal (i.e., r_{12}) direction. At a temperature of 167 °C already the CDF pseudo-color representation clearly shows the main feature in the CDF: two elongated peaks extending in vertical direction. Their height indicates the block height, and their position on the equator is determined by the average gap or block width. We observe that the predominant topological change during remelting is an increase of the average block height with increasing temperature. Thus, assemblies of high blocks are the most stable ones and melt as the latest.

In summary, even the SAXS data from the in-situ remelting experiment are in favor of Strobl's block mechanism for the growth of secondary lamellae in our polypropylene material.

3.6. WAXS at Room Temperature after Oriented Crystallization. After the reported failure of in-situ SAXS/WAXS experiments at least at room temperature WAXS patterns of recrystallized material have been recorded on the advice of one of the reviewers.

The WAXS diagram of the virgin hard-elastic material is well-known.[27,28] Similar to most of the uniaxial polypropylene materials,[30,59] even the hard-elastic polypropylene exhibits a peculiar bimodal WAXS diagram. For a fraction of the crystallites the *c*-axis is oriented in fiber direction, whereas the *a**-axis is pointing in fiber direction for the smaller fraction (0−20%)[60] of the crystallites. Despite its bimodal WAXS diagram, the hard-elastic material shows a uniform orientation of crystalline lamellae in the electron microscope.[27,28] In an atomic force microscopy paper[61] these lamellae are described to consist from crystalline blocks. As to our knowledge, cross-hatched lamellae are not reported for hard-elastic polypropylene.

In order to perform the test, a piece of the original material is exposed to temperature treatment in a DSC apparatus. The temperature program chosen is the same as in the in-situ experiment of isothermal crystallization at 145 °C. After the treatment 2D SAXS and WAXS patterns are recorded on laboratory equipment. In the SAXS pattern (Figure 12a) the cross-pattern from the time-resolved experiments (cf. Figure 5, right row center) is reproduced. The WAXS pattern (Figure 12b) shows a bimodal fiber pattern very similar to the one that is observed and published[27,28] for the virgin hard-elastic material. The only difference is in the lengths of the orientation distribution arcs. In the recrystallized material they are slightly longer.

As compared to our preceding studies of several polyethylenes,[23,40,48,50,62] it appears worth mentioning that in the recrystallization process even the orientation of the crystallites is

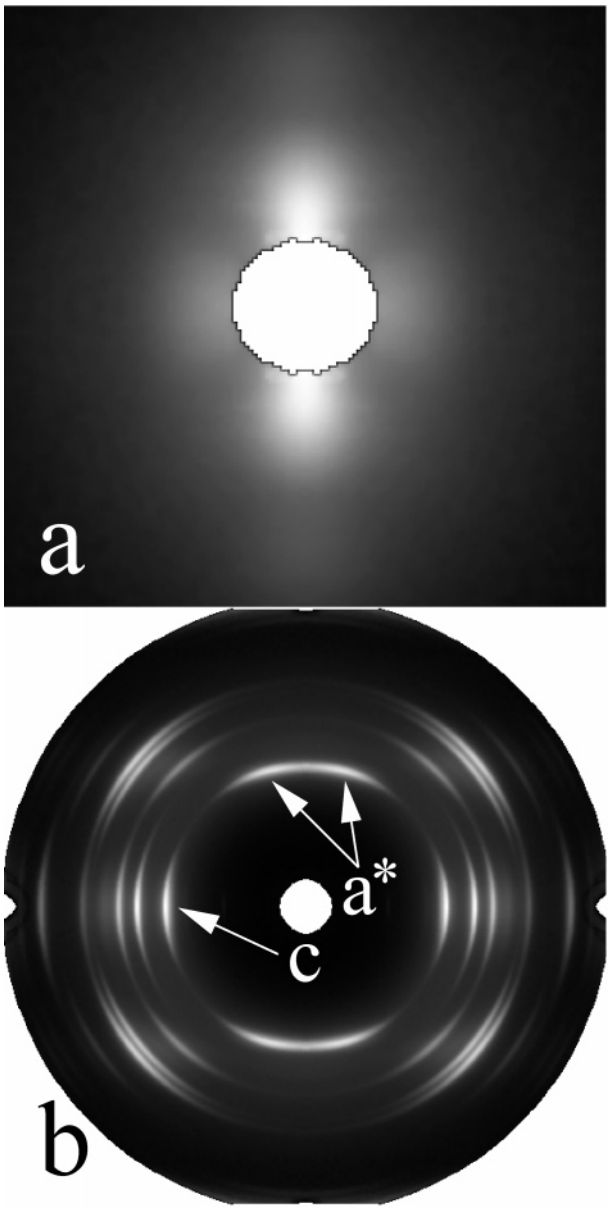

Figure 12. Test of the WAXS orientation related to a recrystallized material showing (a) the SAXS cross pattern. The WAXS pattern (b) shows the same bimodal orientation as the original material with plain lamellar SAXS. The (110) reflections related to *c*-axis oriented crystals and *a**-axis oriented crystals are indicated by arrows.

almost perfectly reproduced. With polyethylene we observed highly oriented primary lamellae made from isotropic crystallites which only gained orientation during the course of the isothermal period. The secondary crystallites which grew after the volume was populated with primary crystals were isotropic, anyway. For polyethylene this mechanism resulted in an ultimate structure at room temperature with isotropic WAXS and anisotropic SAXS.

Recapitulating the result of our polypropylene, the WAXS carried out after the oriented crystallization does not show any substantial difference as compared to the initial state. Thus, it does not help to answer the question if the cross-hatched structure or the block structure model is more favorable. Nevertheless, we plan to carry out a time-resolved WAXS experiment of melting and oriented crystallization of hard-elastic polypropylene in order to answer the question, if both kinds of crystallite orientation vanish and appear simultaneously or not.

4. Conclusions

Compared to polymeric materials previously studied during anisotropic crystallization from a quiescent melt, the polypropylene material presented here exhibits the so-far most-complex mechanisms of nanostructure evolution. Correspondingly complex is the nanostructure in several thousand of analyzed 2D scattering patterns. Whereas the fundamental mechanisms can be identified quite clearly by qualitative observation of scattering patterns and CDFs, the quantitative analysis appears particularly difficult. Thus, the simple peak analysis presented in Figures 7 and 8 is not more than a first approximation. It would be more appropriate to program a multidimensional structural model for each component (lamellae, block assemblies, row assemblies) and then to fit the complex model to the scattering data. In practice, such an analysis will most probably not be developed within the next decade because of the complexity of this task. Thus, the evaluation bottleneck resulting from the streams of high-fidelity scattering data which can be recorded by sensitive detectors at brilliant beamlines is twofold: it does not only comprise the preevaluation and qualitative analysis. Even more serious is the data evaluation bottleneck in the field of a quantitative analysis.

Our quiescent experiments at low undercooling clearly exhibit both primary and secondary crystallization. At least the secondary crystallization is not a simple mechanism but follows the "pathway of building lamellae from blocks" as depicted by Strobl.[16] The fusing mechanism is a surprisingly slow one, and upon reheating imperfectly fused lamellae first decompose into blocks before they melt.

The conditions necessary for the evolution of the block structure in our SAXS experiments are identical to the conditions that are described[9] as typical for the development of the cross-hatched structure found in TEM studies. As shown by us, from a topological point of view both models are closely related to each other. Nevertheless, from the viewpoint of materials science they are differing considerably. The newly appeared issue concerning the results of SAXS and TEM must be relinquished to further investigation.

Acknowledgment. We thank the Hamburg Synchrotron Radiation Laboratory (HASYLAB) for beam time granted in the frame of project II-01-041 and the European Synchrotron Radiation Facility (ESRF), Grenoble, for beam time granted in the frame of project SC 1679. We gratefully acknowledge funding by the Deutsche Forschungsgemeinschaft, project STR 501/4-1. We thank Dr. A. Frömsdorf and N. Schober for the recording of additional WAXS and SAXS patterns. Last but not least we are grateful to all three reviewers for their extensive comments and their requests to extend the study, to demonstrate the CDF method in detail, and their committed discussion of the presented results.

References and Notes

(1) Somani, R. H.; Hsiao, B. S.; Nogales, A.; Srinivas, S.; Tsou, A. H.; Sics, I.; Baltá Calleja, F. J.; Ezquerra, T. A. *Macromolecules* **2000**, *33*, 9385−9394.
(2) Kumaraswamy, G.; Verma, R. K.; Issaian, A. M.; Wang, P.; Kornfield, J. A.; Yeh, F.; Hsiao, B. S.; Olley, R. H. *Polymer* **2000**, *41*, 8931−8940.
(3) Somani, R. H.; Yang, L.; Hsiao, B. S.; Agarwal, P. K.; Fruitwala, H. A.; Tsou, A. H. *Macromolecules* **2002**, *35*, 9096−9104.
(4) Somani, R. H.; Yang, L.; Hsiao, B. H.; Fruitwala, H. *J. Macromol. Sci., Part B: Phys.* **2003**, *B42*, 515−531.
(5) Nogales, A.; Mitchell, G. R. *Polymer* **2005**, *46*, 5615−5620.
(6) Ogino, Y.; Fukushima, H.; Takahashi, N.; Matsuba, G.; Nishida, K.; Kanaya, T. *Macromolecules* **2006**, *39*, 7617−7625.

(7) Balzano, L.; Rastogi, S.; Peters, G. In *Nanotech 2006*; Nano Science and Technology Institute: Cambridge, MA, 2006; Vol. 2, pp 820−823.
(8) Norton, D. R.; Keller, A. *Polymer* **1985**, *26*, 704−716.
(9) Olley, R. H.; Bassett, D. C. *Polymer* **1989**, *30*, 399−409.
(10) Albrecht, T.; Strobl, G. *Macromolecules* **1995**, *28*, 5267−5273.
(11) Wang, Z.-G.; Hsiao, B. S.; Sirota, E. B.; Agarwal, P.; Srinivas, S. *Macromolecules* **2000**, *33*, 978−989.
(12) Dai, P. S.; Cebe, P.; Capel, M.; Alamo, R. G.; Mandelkern, L. *ACS Symp. Ser.* **2000**, *739*, 152−165.
(13) Dai, P. S.; Cebe, P.; Capel, M.; Alamo, R. G.; Mandelkern, L. *J. Appl. Crystallogr.* **2000**, *33*, 714−717.
(14) Ryan, A. J.; Terrill, N. J.; Fairclough, J. P. A. *ACS Symp. Ser.* **2000**, *739*, 201−217.
(15) Heeley, E. L.; Maidens, A. V.; Olmsted, P. D.; Bras, W.; Dolbnya, I. P.; Fairclough, J. P. A.; Terrill, N. J.; Ryan, A. J. *Macromolecules* **2003**, *36*, 3656−3665.
(16) Hugel, T.; Strobl, G.; Thomann, R. *Acta Polym.* **1999**, *50*, 214−217.
(17) Strobl, G. *Prog. Polym. Sci.* **2006**, *31*, 398−442.
(18) Kolb, R.; Wutz, C.; Stribeck, N.; v. Krosigk, G.; Riekel, C. *Polymer* **2001**, *42*, 5257−5266.
(19) Fujiyama, M.; Masada, I.; Mitani, K. *J. Appl. Polym. Sci.* **2000**, *78*, 1751−1762.
(20) Suaphol, P.; Lin, J.-S. *Polymer* **2001**, *42*, 9617−9626.
(21) Cho, K.; Saheb, D. N.; Choi, J.; Yang, H. *Polymer* **2002**, *43*, 1407−1416.
(22) Cho, K.; Saheb, D. N.; Yang, H.; Kang, B.-I.; Kim, J.; Lee, S.-S. *Polymer* **2003**, *44*, 4053−4059.
(23) Stribeck, N.; Almendarez Camarillo, A.; Bayer, R. *Macromol. Chem. Phys.* **2004**, *205*, 1463−1470.
(24) Kristiansen, P. M.; Gress, A.; Hanft, D.; Schmidt, H.-W. *Polymer* **2006**, *47*, 249−253.
(25) Blomenhofer, M.; Ganzleben, S.; Hanft, D.; Schmidt, H.-W.; Kristiansen, M.; Smith, P.; Stoll, K.; Mäder, D.; Hoffmann, K. *Macromolecules* **2005**, *38*, 3688−3695.
(26) Noether, H. D. *Int. J. Polym. Mater.* **1979**, *7*, 57−82.
(27) Sprague, B. S. *J. Macromol. Sci., Phys.* **1973**, *B8*, 157−187.
(28) Noether, H. D.; Whitney, W. *Colloid Polym. Sci.* **1973**, *251*, 991−1005.
(29) Göritz, D.; Müller, F. H. *Colloid Polym. Sci.* **1974**, *252*, 862−870.
(30) Katayama, K.; Amano, T.; Nakamura, K. *Kolloid Z. Z. Polym.* **1968**, *226*, 125−134.
(31) Stribeck, N.; Almendarez Camarillo, A.; Nöchel, U.; Bösecke, P.; Bayer, R. K. *Anal. Bioanal. Chem.* **2007**, *387*, 649−661.
(32) Stribeck, N. *J. Appl. Crystallogr.* **2001**, *34*, 496−503.
(33) Stribeck, N.; Fakirov, S. *Macromolecules* **2001**, *34*, 7758−7761.
(34) Stribeck, N.; Buzdugan, E.; Ghioca, P.; Serban, S.; Gehrke, R. *Macromol. Chem. Phys.* **2002**, *203*, 636−644.
(35) Stribeck, N. *Fibr. Text EE* **2003**, *11*, 33−45.
(36) Stribeck, N. In Fakirov, S., Ed.; *Condensation Thermoplastic Elastomers*; Wiley-VCH: Weinheim, 2005; pp 197−225.
(37) Stribeck, N.; Androsch, R.; Funari, S. S. *Macromol. Chem. Phys.* **2003**, *204*, 1202−1216.
(38) Stribeck, N. *Anal. Bioanal. Chem.* **2003**, *376*, 608−617.
(39) Stribeck, N.; Fakirov, S.; Apostolov, A. A.; Denchev, Z.; Gehrke, R. *Macromol. Chem. Phys.* **2003**, *204*, 1000−1013.
(40) Stribeck, N.; Almendarez Camarillo, A.; Cunis, S.; Bayer, R. K.; Gehrke, R. *Macromol. Chem. Phys.* **2004**, *205*, 1445−1454.
(41) Stribeck, N. *X-Ray Scattering of Soft Matter*; Springer: Heidelberg, 2007.
(42) Stribeck, N.; Almendarez Camarillo, A.; Nöchel, U.; Schroer, C.; Kuhlmann, M.; Roth, S. V.; Gehrke, R.; Bayer, R. K. *Macromol. Chem. Phys.* **2006**, *207*, 1239−1249.
(43) VNI, *pv-wave manuals*, V 7.5 (2001), Boulder, CO.
(44) Ruland, W. *Colloid Polym. Sci.* **1977**, *255*, 417−427.
(45) Vonk, C. G. *Colloid Polym. Sci.* **1979**, *257*, 1021−1032.
(46) Buhmann, M. D. *Acta Numerica* **2000**, *9*, 1−38.
(47) Almendarez Camarillo, A.; Stribeck, N. *Fibres Text. East. Eur.* **2005**, *13*, 27−29.
(48) Almendarez Camarillo, A.; Roth, S. V.; Bösecke, P.; Buchner, S.; Krenn, K.; Gehrke, R.; Stribeck, N. *J. Mater. Sci.*, in press.
(49) Wang, Z.-G.; Phillips, R. A.; Hsiao, B. S. *J. Polym. Sci., Part B: Polym. Phys.* **2000**, *38*, 2580−2590.
(50) Stribeck, N. *Macromol. Chem. Phys.* **2004**, *205*, 1455−1462.
(51) Schultz, J. M.; Lin, J. S.; Hendricks, R. W. *J. Appl. Crystallogr.* **1978**, *11*, 551−557.
(52) Rényi, A. *Sel. Transl. Math. Stat. Prob.* **1963**, *4*, 203−218.
(53) Bonnier, B.; Boyer, D.; Viot, P. *J. Phys. A* **1994**, *27*, 3671−3682.
(54) Evans, J. W. *Rev. Mod. Phys.* **1993**, *65*, 1281−1329.
(55) Hoffman, J. D.; Lauritzen, J. I., Jr.; Passaglia, E.; Ross, G. S.; Frolen, L. J.; Weeks, J. J. *Kolloid Z. Z. Polym.* **1969**, *231*, 564−592.
(56) Stribeck, N.; Funari, S. S. *J. Polym. Sci., Part B: Polym. Phys.* **2003**, *41*, 1947−1954.
(57) Johnson, M. B.; Wilkes, G. L. *J. Appl. Polym. Sci.* **2001**, *81*, 2944−2963.
(58) Xu, J.; Johnson, M.; Wilkes, G. L. *Polymer* **2004**, *45*, 5327−5340.
(59) Compostella, M.; Coen, A.; Bertinotti, F. *Angew. Chem.* **1962**, *74*, 618−624.
(60) Sakthivel, A.; Abhiraman, S. *J. Appl. Polym. Sci.* **1984**, *29*, 4257−4264.
(61) Keith, H. D.; Padden, J. F. J. *J. Appl. Phys.* **1964**, *35*, 1270−1285.
(62) Stribeck, N.; Bösecke, P.; Bayer, R.; Almendarez Camarillo, A. *Prog. Colloid Polym. Sci.* **2005**, *130*, 127−139.
(63) We define the initial cooling rate according to common understanding by the derivative with respect to time of the temperature vs time curve at the exit of the isothermal plateau.

MA070251T